# Elasticity of Hydrated Al-Bearing Stishovite and Post-Stishovite: Implications for Understanding Regional Seismic $V_S$ Anomalies along Subducting Slabs in the Lower Mantle

**Yanyao Zhang[1], Suyu Fu[1]*, Shun-ichiro Karato[2], Takuo Okuchi[3], Stella Chariton[4], Vitali B. Prakapenka[4], Jung-Fu Lin[1]**

[1]Department of Geological Sciences, Jackson School of Geosciences, The University of Texas at Austin, Austin, TX 78712, USA

[2]Department of Earth and Planetary Sciences, Yale University, New Haven, CT 06520, USA

[3]Institute for Integrated Radiation and Nuclear Science, Kyoto University, Osaka 590-0494, Japan

[4]Center for Advanced Radiation Sources, University of Chicago, IL 60637, USA

Corresponding authors: Jung-Fu Lin (afu@jsg.utexas.edu), Yanyao Zhang (yanyaozhang@utexas.edu)

*Current address: School of Earth and Space Exploration, Arizona State University, Tempe, AZ 85287, USA.

**Key Points (≤140 characters for each with no special characters or acronyms):**

- Elastic moduli across the Al,H-bearing post-stishovite transition are derived from high-pressure Raman and X-ray diffraction data
- Stishovite with 1.3 mol% Al and 0.6 mol% H undergoes the post-stishovite transition at ~1060 km depth with -29% $V_s$ anomaly
- $V_S$ reductions across the Al,H-bearing post-stishovite transition can explain regional seismic $V_S$ anomalies along some subducting slabs

## Abstract (<250 words)

Seismic studies have found regional seismic scatterers with -2 to -12% $V_S$ anomalies along some subducting slabs at 700-1900 km depth. The ferroelastic post-stishovite transition in subducted mid-ocean ridge basalt (MORB) has been linked to these seismic features, but compressional and shear wave velocities ($V_P$ and $V_S$) and full elastic moduli ($C_{ij}$) of Al,H-bearing stishovite and post-stishovite at high pressure remain uncertain. Here we have determined Raman shifts of optic modes and equation of state parameters of two hydrated Al-bearing stishovite crystals, Al1.3-$SiO_2$ (1.34 mol% Al and 0.55 mol% H) and Al2.1-$SiO_2$ (2.10 mol% Al and 0.59 mol% H), up to ~70 GPa in diamond anvil cells coupled with Raman spectroscopy and X-ray diffraction. The experimental data are modeled using a pseudoproper Landau theory to derive full elastic moduli ($C_{ij}$) and sound velocities across the post-stishovite transition at high pressure. The Al and H dissolution in stishovite significantly reduces the transition pressure to 21.1 GPa in Al1.3-$SiO_2$ and to 16.1 GPa in Al2.1-$SiO_2$, where the transition is manifested by approximately 29% $V_S$ reduction. Considering that stishovite with approximately 1.3 mol% Al and 0.6 mol% H could account for 20 vol% in subducted MORB at top lower mantle depths, the Al,H-bearing post-stishovite transition with a Clapeyron slope of 65 K/GPa would occur at about 1060 km depth with -7(4)% $V_S$ anomaly. The $V_S$ anomalies across the Al,H-bearing post-stishovite transition can help explain the depth-dependent seismically-observed $V_S$ anomalies along some subducting slabs in the top to mid lower-mantle depths including the Tonga subducting slabs.



## Plain Language Summary (<200 words)

Seismologists have found that shear wave travels 2-12% slower along some regions of subducting slabs at 700-1900 km depths than the surrounding lower mantle. This observation cannot be explained by the presence of cold subducting oceanic crusts, but the transition from stishovite to post-stishovite could be a possible cause. Stishovite is a high-pressure dense silica polymorph that makes up about one fifth volume of subducting mid-ocean ridge basalt in the lower mantle. We designed high-pressure Raman spectroscopy experiments to probe the lattice vibration modes and X-ray diffraction to measure lattice parameters of Al,H-bearing stishovite and post-stishovite. These results are used to evaluate the speed of sound across the post-stishovite transition. Our study shows that the shear wave velocity of stishovite with 1.3-2.1 mol% Al and 0.5-0.6 mol% H significantly slows down by -29 % at 16-21 GPa. If one quarter volume of the subducting oceanic crust is made of stishovite with 1.3 mol% Al and 0.6 mol% H, the velocity reduction across the transition could be ~7% at ~1060 km depth. Regional seismic observations of $V_S$ anomalies along some subducting slabs in the top to mid lower mantle can be explained by the presence of the Al,H-bearing post-stishovite transition.

## 1. Introduction

Seismic tomographic studies have revealed wide-spread stagnant slabs in the mantle beneath subduction zones (Fukao & Obayashi, 2013). The subducting slabs contain Mid-Ocean Ridge Basalt (MORB) and other crustal and sedimentary materials that are chemically and physically distinct from the lithospheric mantle (Ringwood, 1975). As slab subduction occurs deeper into the lower mantle, basaltic materials are expected to exhibit distinct mineralogy and physical properties that may be revealed seismically (Ishii et al., 2019; Rost et al., 2008). Compared with the mantle lithosphere of approximately 100-200 km thick, the oceanic crust is only ~7 km thick so interpretations of seismic images for the subducting MORB materials in the lower mantle have been challenging. Specifically, global seismic tomography has a length scale resolution of hundreds of kilometers that could not be used to detect the subducted basalt (or eclogite) in the mantle (Fukao & Obayashi, 2013). On the other hand, analyses of short period seismic-wave scattering can provide a much better spatial resolution in the order of ~10 km in the mantle (Rost et al., 2008). Insofar, these short period seismic studies have revealed the occurrence of many regional seismic scatterers with a number of distinct features: (1) slower shear wave velocity ($V_S$) anomaly up to ~12 % reduction, no significant compressional wave velocity ($V_P$) anomaly, and higher density anomaly up to ~9% enhancement at 700-1900 km depth in some regions (Niu, 2014; Niu et al., 2003); (2) planar geometry with several to tens of kilometers in thickness and tens to hundreds of kilometers in size; (3) occurrence within or beneath the subduction slab along the circum-Pacific region, but the frequency of observations decreases from top to mid lower mantle (Haugland et al., 2017; Kaneshima, 2019; Li & Yuen, 2014; Vinnik et al., 2001). These features are thought to be indicative of the presence of ancient subducted basalts in the lower mantle (Kaneshima & Helffrich, 1999).

To decipher the aforementioned seismic observations at depths, sound velocities and densities of major constituent minerals at relevant mantle pressure-temperature (*P*-*T*) conditions of the subducted slabs are critically needed. Subducted MORB materials at the upper part of the lower mantle are expected to contain approximately 20 vol% stishovite, 30 vol% $CaFe_2O_4$-type phase or new hexagonal phase (CF or NAL), 30 vol% bridgmanite (Bgm), and 20 vol% Ca-perovskite (CaPv) (Ishii et al., 2019). Previous studies have shown that sound velocities of these phases except stishovite fall between those of bridgmanite and ferropericlase, the two most abundant minerals in a pyrolite compositional model, in the lower mantle (Gréaux et al., 2019; Wu et al., 2016; Xu et al., 2008; Yang et al., 2015). That is, their velocity characteristics could not be used to reconcile the observations of small-scale seismic $V_S$ anomalies along subducting slabs in the lower mantle.

However, their occurrence could contribute to seismic observations of enhanced densities in some regions (Hirose et al., 2005; Niu, 2014; Niu et al., 2003; Sun et al., 2016). On the other hand, the rutile-type stishovite displays much higher sound velocities than typical mantle minerals (Yang & Wu, 2014; Zhang et al., 2021), although its density is similar to that of mineral aggregates in a pyrolite composition (Fischer et al., 2018; Irifune et al., 2010). Stishovite undergoes a pseudoproper ferroelastic transition to a $CaCl_2$-type post-stishovite phase with a spontaneous strain (Carpenter et al., 2000; Hemley et al., 2000). For pure-endmember stishovite ($SiO_2$), the distortion transition occurs at 55 GPa and 300 K and is associated with a drastic $V_S$ reduction of -26% and a mild $V_P$ reduction of -10%, but the density continuously increases with increasing pressure (Zhang et al., 2021). It has been theoretically shown that subducted MORB with 20 vol% stishovite undergoing the post-stishovite transition could produce a $V_S$ reduction of up to ~6.5% and a $V_P$ reduction of up to ~1.5% at the mid-lower-mantle depth that can help explain seismic wave velocities (Wang et al., 2020). However, the post-stishovite transition has a positive Clapeyron slope of 65 K/GPa and would occur at ~1800 km depth at relevant *P*-*T* conditions of a cold subducting slab (77 GPa and 1706 K) (Fischer et al., 2018). The transition depth is thus too deep to be consistent with these aforementioned regional seismic $V_S$ anomalies at shallower lower mantle depths.

Based on previous geochemical and petrological studies (Gale et al., 2013), subducted MORB materials can contain ~10-19 wt% alumina (or ~4.3-8.1 mol%) which can partition into stishovite crystals. Multi-anvil apparatus experiments on element partitioning in a basaltic system have revealed that the Al content in stishovite increases from ~0.5 mol% at 22 GPa to ~1.5 mol% at 33 GPa (Ishii et al., 2019; Ono et al., 2001). Additionally, chemical analysis of mineral inclusions in natural diamonds from the subducted eclogitic assemblage also shows the presence of nearly Al-free silica (≤ 0.06 mol% Al) in association with $Al_2SiO_5$ phase (Zedgenizov et al., 2015). This indicates the possible presence of Al-bearing stishovite at lower-mantle depths, although naturally-occurring Al-bearing stishovite has not been reported. In addition to the Al substitution, subducting slabs can contain a small amount of water in hydrous or nominally anhydrous minerals (NAMs) in the mantle. In multi-anvil apparatus experiments, Fourier-transform infrared spectroscopy (FTIR) analyses showed that Al-bearing stishovite crystals contain approximately 0.03-0.67 mol% H at 20-26 GPa and 1473-2073 K conditions (Litasov et al., 2007).

The $Al^{3+}$ and/or $H^+$ incorporation in stishovite can reduce the post-stishovite transition pressure to the depth range more consistent with the seismic observations of the regional $V_S$ anomalies in the shallow lower mantle (Lakshtanov et al., 2007b; Umemoto et al., 2016). Although full elasticity of pure stishovite and post-stishovite and the effect of Al on the post-stishovite transition pressure have been relatively well investigated (Asahara et al., 2013; Karki et al., 1997; Lakshtanov et al., 2007b; Li et al., 1996; Shieh et al., 2002; Yang & Wu, 2014; Zhang et al., 2021), elasticity data of hydrated Al-bearing stishovite across the post-stishovite transition remains largely unexplored (Bolfan-Casanova et al., 2009; Gréaux et al., 2016; Lakshtanov et al., 2007a). This is mainly due to the technical difficulty in measuring sound velocities and reliably deriving full elastic moduli ($C_{ij}$) of the stishovite crystal at high pressure (Zhang et al., 2021). Alternatively, high-pressure experimental results on Raman shifts of optic modes and equations of state (EOS) parameters across the post-stishovite transition can be used to evaluate full $C_{ij}$ using Landau theory modeling (Carpenter et al., 2000). The full $C_{ij}$ data can then be used to calculate sound velocities and other elastic parameters across the post-stishovite transition as a function of pressure.

In this study, we have measured Raman shifts of major optic modes and lattice parameters of two hydrated Al-bearing stishovite single crystals, Al1.3-$SiO_2$ (1.34 mol% Al and 0.55 mol% H) and Al2.1-$SiO_2$ (2.10 mol% Al and 0.59 mol% H), up to ~70 GPa in high-pressure diamond anvil cells. The experimental data are modeled with a pseudoproper Landau theory in which some Landau parameters have been well constrained using a recent experimental elasticity study of stishovite at high pressure (Zhang et al., 2021). These combined experimental and modeling approaches allow us to determine full elastic properties of the Al-bearing stishovite, including $C_{ij}$, adiabatic bulk and shear modulus ($K_S$ and $\mu$), aggregate sound velocities ($V_S$ and $V_P$), and Poisson's ratio ($\nu$), across the post-stishovite transition at high pressure. Our results show that the post-stishovite transition occurs at 21.1 GPa in Al1.3-$SiO_2$ and 16.1 GPa in Al2.1-$SiO_2$, where the $B_{1g}$ optic mode softens and the elastic moduli $C_{11}$ and $C_{12}$ merge together. The full $C_{ij}$ and sound veloicities of hydrated Al-bearing stishovite and post-stishovite from high-pressure Raman and X-ray diffraction measurements are used to provide new constraints on Al/H-dependent post-stishovite transition and associated velocity change at high *P*-*T*. Assuming that subducted MORB materials contain 20 vol% stishovite with 1.3 mol% Al and 0.6 mol% H, our results show that the post-stishovite transition can exhibit a $V_S$ reduction of -7(4)%. We have further modeled the $V_S$ anomaly of the post-stishovite transition as a function of Al contents at high *P*-*T*. These results are compared with regional seismic observations in some selected subduction zone settings including the Tonga slab. Our results provide new insights into the regional seismic $V_S$ anomalies that can be explained by the hydrated Al-bearing post-stishovite transition from the top-to-mid lower mantle.

## 2. Experimental details

Al-bearing stishovite crystals were synthesized at the Institute for Planetary Materials at Okayama University. Two starting samples were prepared by mixing silica powder of 99.99%

purity with 10 wt% gibbsite $Al(OH)_3$ in run# 5K3302 and with 13 wt% gibbsite $Al(OH)_3$ in run# 1K2965. Each starting mixture was loaded into a platinum capsule of 4 mm in length and 2 mm in outer diameter. The sample assemblage in run# 5K3302 with a $LaCrO_3$ heater was compressed to 20 GPa and then heated to 1973 K for 16.5 hours in a 5000-ton Kawai-type multi-anvil apparatus. The assemblage in run# 1K2965 with the same type of heater was compressed to 19.2 GPa and heated to 1973 K for 7 hours using a 1000-ton Kawai-type multi-anvil apparatus. Detailed information about the sample assemblage and apparatus conditions can be found in the literature (Okuchi et al., 2015; Xu et al., 2017). Stishovite crystals extracted from the Pt capsules are anhedral to subhedral in shape and are about tens to hundreds of micrometers in size under an optical microscope. A few crystals of approximately 100-200 μm in diameters were selected for compositional analysis using a JEOL Electron Microprobe (EPMA) and a Scanning Electron Microscopy with Energy Dispersive X-Ray Spectroscopy (SEM/EDS) in the Department of Geological Sciences at the University of Texas at Austin (UT Austin). Chemical mappings on Si, Al, and O elements of the crystals show compositional homogeneities throughout the crystals (Figure S1). Analysis of Wavelength-Dispersive Spectroscopy (WDS) results shows Al contents of 1.34(2) mol% (or 3.43(6) wt% $Al_2O_3$ averaged from 5 analyses) in the Al1.3-$SiO_2$ crystal from run# 5K3302 and 2.10(2) mol% (or 5.37(4) wt% $Al_2O_3$ averaged from 8 analyses) in Al2.1-$SiO_2$ from run# 1K2965 (Table S1). Other elements were below the detection limit of the analytical techniques used here.

Synchrotron X-ray diffraction (XRD) measurements are used to determine the crystal structure and lattice parameters of the crystals at the beamline 13ID-D of the GSECARS, Advanced Photon Source (APS), Argonne National Laboratory. A few Al1.3-$SiO_2$ and Al2.1-$SiO_2$ crystals were polished down to approximately 10-15 μm thick platelets, and then loaded into a sample chamber in a diamond anvil cell with a pair of 300 μm flat culets. The sample chamber was made of a rhenium gasket with an initial thickness of 260 μm that was pre-indented to ~32 μm thickness and subsequently a hole of 190 μm diameter was drilled in it. Au powder (Goodfellow; 99.95% purity) of 5-10 μm big was also loaded next to the crystals in the sample chamber and used as the pressure calibrant (Fei et al., 2007). Neon pressure medium was loaded into the sample chamber using the gas loading system in the Mineral Physics Laboratory, UT Austin. The neon medium provides a quasi-hydrostatic environment in the sample chamber within our investigated pressure range (Kingma et al., 1995). An incident X-ray beam with a wavelength of 0.3344 Å was focused down a beam size of ~3×3 $\mu m^2$ (FWHM) at the sample position where the diffracted signals were collected by a CdTe Pilatus 1M detector. During the data collection, the sample stage was rotated ±15° about its vertical axis to cover more reflection spots. The collected images were further integrated into one-dimensional spectra using the DIOPTAS software (Prescher & Prakapenka, 2015). Pressure uncertainties were evaluated from the EOS of Au in the experiments.

High-pressure Raman measurements were performed using a Renishaw InVia Raman spectroscopy system at the Mineral Physics Laboratory, UT Austin. A pair of anvils with 300 μm flat culets and ultralow fluorescence background were selected for the experiments. Similar to the sample preparation in aforementioned XRD experiments, Al1.3-$SiO_2$ and Al2.1-$SiO_2$ platelets of 10-15 μm thick and 20-40 μm big were loaded into a sample chamber with Ne pressure medium. A few ruby spheres were also loaded in the chamber and used as the pressure calibrant (Fei et al., 2007). The Raman system is equipped with a green excitation laser of 532 nm wavelength, a grating of 2400-line/mm, and a spectral resolution of 1.2 $cm^{-1}$. The system was calibrated using the Raman peak of a reference Si crystal at 520 $cm^{-1}$ before high-pressure measurements. Each Raman spectrum was collected using a 20X objective with a focused beamsize of ~2-3 μm, an exposure time of 15 s, and 20-30 accumulations. Pressure uncertainties of the experiments were evaluated from multiple ruby fluorescence measurements before and after each set of the Raman collection. Water contents in the crystals are also evaluated using unpolarized FTIR spectra taken in a Thermo Electron 6700 FTIR spectrometer with a connected FTIR Continuum microscope in the Department of Earth Sciences at the National Cheng Kung University. Raman spectra of the OH-stretching band regions of the Al-bearing stishovite crystals were also measured at ambient conditions.

## 3. Results

### 3.1. Al and H substitution in the rutile-type stishovite

Combined results of FTIR, Raman, electron microprobe and XRD spectral measurements are useful to examine Al and H substitutions in hydrated Al-bearing stishovite crystal structure (Figure 1). Analysis of XRD spectra of the synthesized crystals reveals the tetragonal rutile-type crystal structure with $P4_2/mnm$ space group at ambient conditions. Refined lattice parameters of the Al1.3-$SiO_2$ crystal are $a$ = 4.1963(8) Å, $c$ = 2.6723(4) Å, and $V$ = 47.06(2) Å$^3$ while the Al2.1-$SiO_2$ crystal displays $a$ = 4.2025(9) Å, $c$ = 2.6788(16) Å, and $V$ = 47.31(2) Å$^3$. Our results are consistent with the literature data in which the unit-cell volume of stishovite linearly expands with increasing Al content (Figure 1c) (Lakshtanov et al., 2007b; Litasov et al., 2007). The lattice expansion can be mainly related to the coupled $2Al^{3+}$ and $O_V^{2+}$ (oxygen vacancy) substitution for $2Si^{4+}$ in stishovite (Lakshtanov et al., 2007a). On the other hand, analysis of unpolarized FTIR and Raman spectra shows three major OH-stretching bands at ~2660, ~3140, and ~3410 cm$^{-1}$, consistent with literature data (Figures 1a and 1b) (Litasov et al., 2007). The strongest FTIR absorption band at 3140 cm$^{-1}$ is also extremely intense in Raman measurements, revealing itself as an active FTIR and Raman mode. This is also the case for the mode at 2660 $cm^{-1}$. The occurrence of the bands has been explained to be indicative of the coupled $Al^{3+}$ + $H^{+}$ and/or pure $4H^{+}$ substitution for $Si^{4+}$ in the structure, which are also expected to contribute to the expansion of the lattice (Nisr et al., 2017; Spektor et al., 2011). The water content $C_{OH}$ of the crystals in the unpolarized spectra can be determined using a calibration method by Paterson (1982):

$$C_{OH} = \frac{X_i}{150\gamma} \int \frac{k(\tilde{\nu})}{(3780 - \tilde{\nu})} d\nu \tag{1}$$

where $X_i$ is the density factor, $X_i = 9/d \times 10^6$, with the mineral density $d$ as 4237 g/l and 4211 g/l for Al1.3-$SiO_2$ and Al2.1-$SiO_2$, respectively; $\gamma$ is the orientation factor which is set as 1/3 for the unpolarized measurements; $k(\tilde{\nu})$ is an absorption in $cm^{-1}$ at each wavenumber $\tilde{\nu}$ in $cm^{-1}$. After subtracting the background and normalizing the sample thickness to 1 cm, the water content in Al1.3-$SiO_2$ and Al2.1-$SiO_2$ crystals are determined as 0.55(11) mol% H (or 0.25(5) wt% $H_2O$) and 0.59(11) mol% H (or 0.27(5) wt% $H_2O$), respectively. Together with chemical analysis results, the molar ratios of Al/H in these crystals are thus 2.4(7):1 and 3.5(8):1. These numbers are close to 2:1 and 3:1 ratio, but much larger than 1:1 ratio for the coupled $Al^{3+}$ + $H^{+}$ substitution mechanism proposed previously (Pawley et al., 1993) (Figure 1d). These indicate that $2Al^{3+} + O_V^{2+} \leftrightarrow 2Si^{4+}$ mechanism is most abundant in our Al-bearing stishovite crystals to expand the lattice, while the $Al^{3+} + H^{+} \leftrightarrow Si^{4+}$ mechanism can help facilitate water incorporation into stishovite.

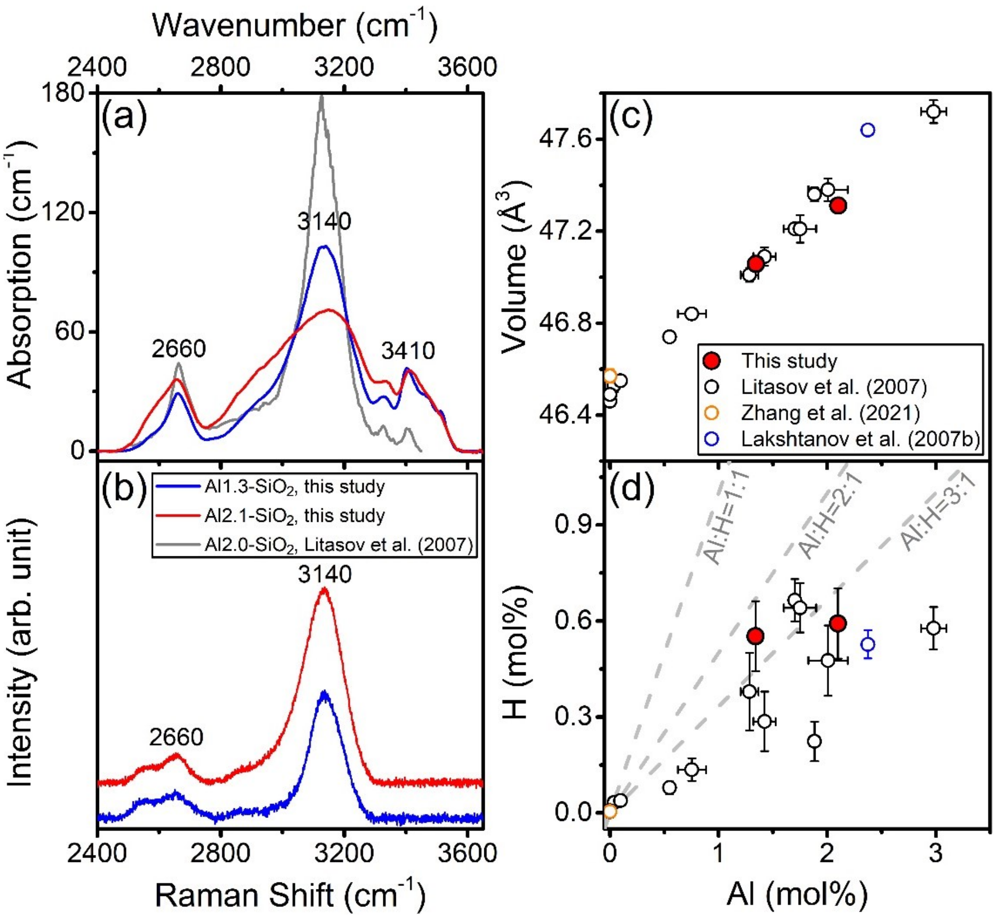


**Figure 1.** Characterizations of hydrated Al-bearing stishovite crystals. (a) and (b) show OH-stretching bands in Al1.3-$SiO_2$ (blue) and Al2.1-$SiO_2$ (red). (a) Representative unpolarized FTIR spectra; (b) representative unpolarized Raman spectra. Wavenumbers and Raman shifts of OH-stretching bands were fitted and labeled next to major peaks in (a) and (b), respectively. (c) Unit-cell volume of stishovite as a function of Al content in mol% at ambient conditions. (d) H content as a function of Al content in mol% in stishovite. Gray dashed lines show three different Al/H ratios. Literature data are plotted for comparison (Lakshtanov et al., 2007b; Litasov et al., 2007; Zhang et al., 2021).

### 3.2. High-pressure Raman shifts of major optic modes across the post-stishovite transition

Analyses of the Raman spectra of the crystals at ambient conditions show four intense optic Raman bands at 226, 583, 748, and 960 cm$^{-1}$ in Al1.3-$SiO_2$ and at 224, 579, 744, and 957 cm$^{-1}$ in

Al2.1-$SiO_2$. After taking the Al substitution effects into account, these peaks can be assigned to $B_{1g}$, $E_g$, $A_{1g}$, and $B_{2g}$ modes of the rutile-type stishovite, respectively (Kingma et al., 1995). The $B_{1g}$, $E_g$, and $A_{1g}$ peaks can be well detected at high pressure, but the $B_{2g}$ mode was blocked by the background of the diamond anvil (Tables S2-S4). Raman shifts of $E_g$ and $A_{1g}$ modes increase with increasing pressure whereas the Raman shifts of the $B_{1g}$ mode decrease with increasing pressure (Figure 2). The trends and slopes of these Raman shifts are consistent with that of pure $SiO_2$ stishovite at high pressure (Kingma et al., 1995; Zhang et al., 2021). Crossing into the $CaCl_2$-type post-stishovite phase, the $B_{1g}$ and $A_{1g}$ evolves into two $A_g$ modes but splitting of $E_g$ mode into $B_{2g}$ and $B_{3g}$ modes was not observed due to background of the diamond anvil. Raman shifts of the $A_g$ modes in the post-stishovite phase increase with increasing pressure, but the slope is shallower than that in pure $SiO_2$ stishovite (Figure 2c). Most importantly, the pressure-dependence of the stishovite's $B_{1g}$ mode becomes positive in the post-stishovite's $A_g$ mode across the post-stishovite transition. A satellite band, denoted as $A_g$*, in the Al1.3-$SiO_2$ crystal occurs between 21.1-36.5 GPa (Figures 2a and 2c) with Raman shift behavior similar to the $A_g$ mode, but the kink occurs at approximately 28 GPa. The occurrence of the satellite peak may be due to local clusters of Al-poor regions where the local domains can resist the shear-driven transition to a higher pressure. This phenomenon across the ferroelastic transition has been reported in other binary systems (Salje, 1990).

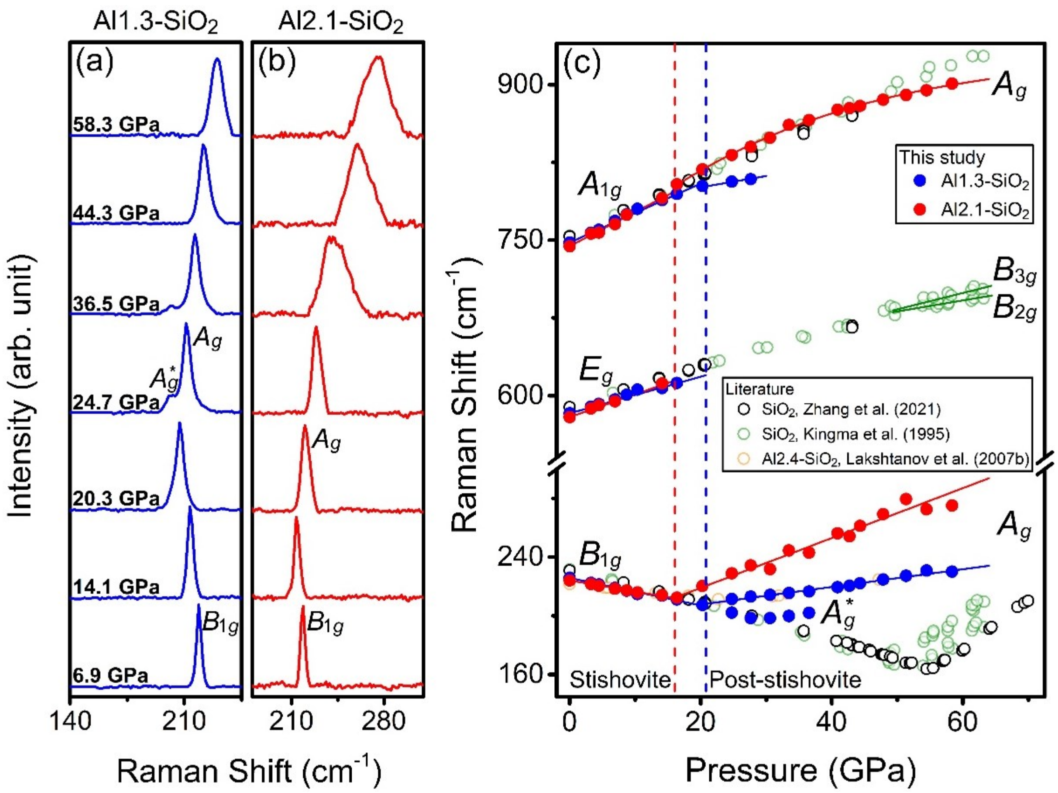


**Figure 2.** Raman shifts of Al-bearing stishovite and post-stishovite phases at high pressure. (a) and (b) are representative Raman spectra of Al1.3-$SiO_2$ and Al2.1-$SiO_2$, respectively, with the $B_{1g}$ optic mode in stishovite and the $A_g$ and $A_g^*$ modes in post-stishovite. (c) Pressure-dependent Raman shifts for Raman modes of stishovite ($B_{1g}$, $E_g$, $A_{1g}$) and post-stishovite ($A_g$, $A_g^*$, $B_{2g}$, $B_{3g}$). Solid lines are best linear or quadratic fits to our experimental data. Error bars are smaller than the symbols and are not shown for figure clarity. Previous studies on stishovite crystals with pure $SiO_2$ (Al free) and Al2.4-$SiO_2$ (2.4 mol% Al) compositions are plotted as open circles for comparison (Kingma et al., 1995; Lakshtanov et al., 2007b; Zhang et al., 2021). Vertical dashed lines show the transition pressure for each composition with the same color as the corresponding data in (a) or (b).

### 3.3. Lattice parameters across the post-stishovite transition

Analysis of the high-pressure XRD spectra from Al1.3-$SiO_2$ and Al2.1-$SiO_2$ crystals shows 10-15 reflections in the tetragonal stishovite phase within 2θ range from 6° to 24° (Figures 3a and 3b; Tables S5 and S6). The analyzed lattice parameters indicate that lengths of *a* and *c* axis and unit-cell volume (*V*) decrease with increasing pressure with slopes consistent with that in pure-endmember stishovite (Figures 3c and 3d). With increasing pressure, some representative diffraction peaks in the tetragonal structure split into the orthorhombic post-stishovite structure with *Pnnm* space group at 21.1 GPa for Al1.3-$SiO_2$ and 16.1 GPa for Al2.1-$SiO_2$. Specifically, tetragonal 211 and 311 reflections in Miller indices split into pairs of orthorhombic (211 and 121) and (311 and 131) reflections, respectively, in Al1.3-$SiO_2$ crystal (Figure 3a). Similarly, splitting of tetragonal 210, 211, 310, 311, 320, 410, 411, and 420 reflections were observed in Al2.1-$SiO_2$ crystal (Figure 3b). These mean that the *a*-axis of the tetragonal stishovite splits into *a*- and *b*-axis of orthorhombic post-stishovite at high pressure. Axial and bulk incompressibilities of the stishovite and post-stishovite phases at high pressure were further evaluated using the Birch-Murnagham EOS (Birch, 1947) (Table S7). Isothermal bulk modulus ($K_{T0}$) of Al1.3-$SiO_2$ and Al2.1-$SiO_2$ crystals at ambient conditions is lower than that in pure $SiO_2$ stishovite, but higher than that in pure $SiO_2$ post-stishovite. These indicate that the Al and H substitution softens the tetragonal structure in stishovite but stiffens the orthorhombic structure in post-stishovite.

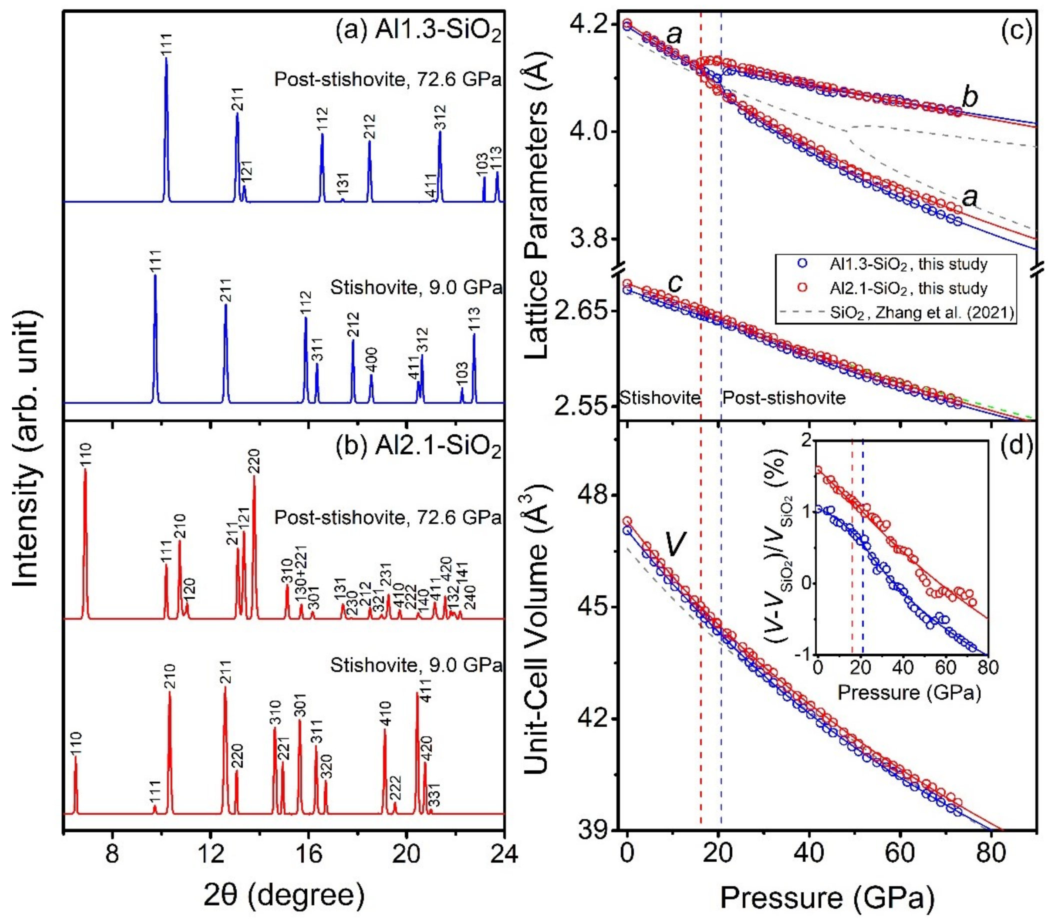


**Figure 3.** X-ray diffraction and equation of state results of hydrated Al-bearing stishovite and post-stishovite at high pressure. (a) and (b) are representative XRD patterns for Al1.3-$SiO_2$ and Al2.1-$SiO_2$ crystals, respectively, at 9.0 GPa for the stishovite phase and at 72.6 GPa for the post-stishovite phase. Miller indices hkl labeled next to identified diffraction peaks are used to calculate lattice parameters and unit cell volumes in (c) and (d). The occurrence of the post-stishovite phase is most visible in the splitting of some reflection peaks in the stishovite phase across the transition, such as a splitting of the 211 reflection into a pair of 211 and 121 reflections. (c) and (d) show lattice parameters and unit-cell volumes, respectively, of the stishovite and post-stishovite phases in Al1.3-$SiO_2$ (blue open circles) and Al2.1-$SiO_2$ (red open circles) at high pressure. Corresponding solid lines show the best fits using the axial incompressibility or the Birch-Murnaghan equation of state (Birch, 1947). The insert panel shows unit-cell volume variations of the Al-bearing crystals at high pressure with respect to that of the endmember $SiO_2$ by Zhang et al. (2021). Vertical dashed lines show the transition pressures.

## 4. Discussion

### 4.1. Landau theory modeling of the elasticity across the post-stishovite transition

Our high-pressure Raman and XRD results are used to derive full $C_{ij}$ and sound velocities of the stishovite and post-stishovite phases. We used a pseudoproper-type Landau free energy expansion, where the order parameter $Q$ is related to the $B_{1g}$ soft optic mode and is coupled bilinearly with the symmetry-breaking spontaneous strain (Carpenter et al., 2000). In the modeling, a number of Landau parameters need to be well evaluated in order to reliably derive the full elastic moduli. These parameters include $P_C^*$, critical pressure ($P_C$), bare elastic moduli ($C_{ij0}^0$), pressure derivatives of $C_{ij0}^0$ ($C_{ij}^{0\prime}$), coupling coefficients ($\lambda_i$), and normal Landau coefficients ($a$ and $b$). To start with, the intersection of the two linear fits to the squared Raman shifts of the $B_{1g}$ and $A_g$ modes as a function of pressure gives the $P_C^*$ value at 21.1(6) GPa for Al1.3-$SiO_2$ and at 16.1(4) GPa for Al2.1-$SiO_2$ (Figure 4a). Extrapolation of the $B_{1g}$ linear fit to zero Raman shift yields the $P_C$ value where the optic mode becomes imaginary. Additionally, the $C_{ij0}^0$ can be calculated from literature $C_{ij0}$ data of stishovite at ambient conditions after taking into account of the linear Al effect on the $C_{ij0}$ in stishovite (Lakshtanov et al., 2007a). Since the pressure-dependent slopes for Raman shifts and lattice parameters are very similar in Al-bearing and pure $SiO_2$ stishovite (Figures 2c, 3c, and 3d), the $C_{ij}^0$ slope, the pressure derivatives of $C_{ij}^0$ ($C_{ij}^{0\prime}$), of the experimentally-determined values for pure $SiO_2$ endmember in a recent study (Zhang et al., 2021) can be used for the Al-bearing stishovite. The exception here is for the $C_{11}^{0\prime}$ and $C_{12}^{0\prime}$ that can be affected by the shear softening and the transition pressure such that these two parameters for the Al-bearing stishovite need to be evaluated in the modeling. Moreover, the coupling coefficients $\lambda_4$ and $\lambda_6$ are also set to those in the pure $SiO_2$ endmember because they are related to the spontaneous strains $e_4$, $e_5$, and $e_6$ that remain zero in the post-stishovite phase regardless of the Al and H content due to the nature of the ferroelastic transition (Carpenter et al., 2000). In short, six parameters (coupling coefficients $\lambda_1$ and $\lambda_3$, Landau coefficients $a$ and $b$, $C_{11}^{0\prime}$ and $C_{12}^{0\prime}$) are evaluated in our modeling using the Al and H dependent spontaneous strains $e_1$, $e_2$, and $e_3$ at high pressures that can be calculated from the lattice paremeters (Figure 4b):

$$e_1 = \frac{a_{Pst} - a_{St}}{a_{St}}, e_2 = \frac{b_{Pst} - a_{St}}{a_{St}}, e_3 = \frac{c_{Pst} - c_{St}}{c_{St}} \quad (2)$$

where $a_{Pst}$, $b_{Pst}$, and $c_{Pst}$ are lattice parameters of post-stishovite (*Pst*) at high pressure; $a_{St}$ and $c_{St}$ are the extrapolated lattice parameters of stishovite (*St*) at the same pressure. With all these Landau parameters determined (Table 1), the full set of $C_{ij}$ of the stishovite and post-stishovite phases at high pressure can be calculated using the $C_{ij}$ expressions in Carpenter et al. (2000). The $V_S$ and $V_P$ values of the phases at each given pressure are calculated using the following equations:

$$V_P = \sqrt{\left(K_S + \frac{4}{3}\mu\right)/\rho}, V_S = \sqrt{\mu/\rho} \quad (3)$$

The Poisson's ratio $\nu$, a key seismic parameter reflecting the $V_P$ and $V_S$ ratio, are also calculated using the following equation:

$$\nu = \frac{1}{2}\left[\left(\frac{V_P}{V_S}\right)^2 - 2\right] / \left[\left(\frac{V_P}{V_S}\right)^2 - 1\right] \quad (4)$$

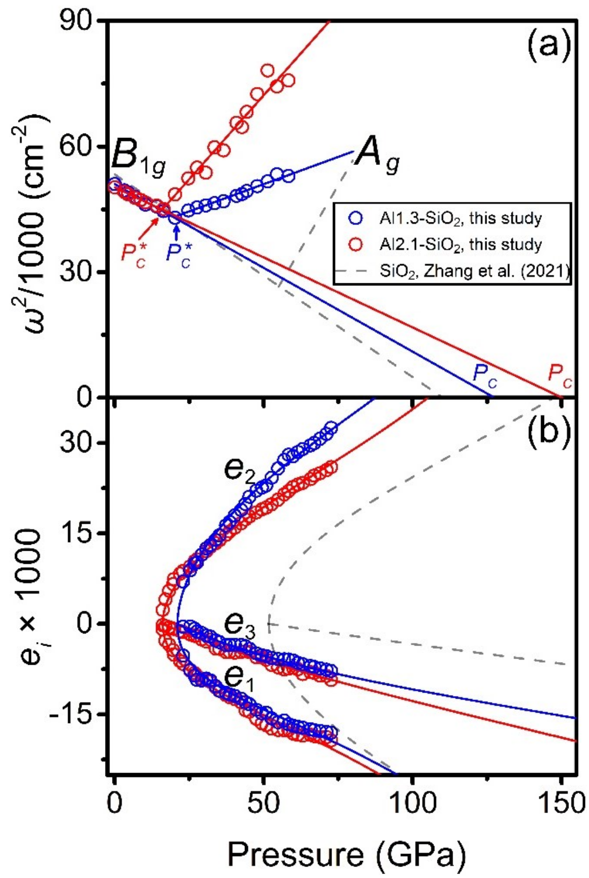


**Figure 4.** Landau theory modeling of the post-stishovite transition in hydrated Al-bearing stishovite. (a) Squared Raman shifts of $B_{1g}$→$A_g$ modes $\omega^2$ divided by 1000 ($\omega^2$/1000). The kink in the Raman shift slope reflects the post-stishovite transition pressure $P_C^*$ for each composition, while the linear extrapolation on $\omega^2$/1000 of the $B_{1g}$ mode to zero yields the critical pressure $P_C$. (b) Spontaneous strains $e_i$ multiplied by 1000 ($e_i$ × 1000; $i$ = 1, 2, 3). Blue and red circles are experimental data on Al1.3-$SiO_2$ and Al2.1-$SiO_2$, respectively, while corresponding lines are best fits. Literature results on endmember $SiO_2$ are shown as gray dashed lines (Zhang et al., 2021).

**Table 1** Landau model parameters for the stishovite to post-stishovite transition

| Compositions | Al1.3-$SiO_2$ 0.7 mol% $H^+$ | Al2.1-$SiO_2$ 0.8 mol% $H^+$ | $SiO_2$ 0.004 mol% $H^+$ |
|---|---|---|---|
| References | This study | This study | Zhang et al. (2021) |
| $P_C^*$, GPa | 21.1(6) | 16.1(4) | 55.0(10) |
| $(P_C - P_C^*)$, GPa | 105.7(38) | 134.3(65) | 55.2(10) |
| $a$ | -0.0512(49) | -0.0467(45) | -0.0501(29) |
| $b$, GPa | 10.5(12) | 10.6(14) | 11 |
| $\lambda_1$, GPa | -4.9(3) | -5.5(2) | 11.03(85) |
| $\lambda_2$, GPa | 60.5 | 78.5 | 27.61 |
| $\lambda_3$, GPa | 12.6(13) | 12.2(11) | 16.79(92) |
| $\lambda_4$, GPa | 18.94 | 18.94 | 18.94(31) |
| $\lambda_6$, GPa | 15.15 | 15.15 | 15.15(22) |
| $C_{110}^0$, GPa | 999 | 1302 | 592.3 |
| $C_{11}^{0\prime}$[a] | 10.0(9) | 9.5(9) | 10.80(47) |
| $C_{120}^0$, GPa | -375 | -693 | 57.9 |
| $C_{12}^{0\prime}$[a] | 9.9(7) | 10.4(8) | 8.81(63) |
| $C_{130}^0$, GPa | 190.6 | 189.2 | 193.0 |
| $C_{13}^{0\prime}$ | 2.91 | 2.91 | 2.91(27) |
| $C_{330}^0$, GPa | 743.5 | 734.1 | 760.2 |
| $C_{33}^{0\prime}$ | 7.07 | 7.07 | 7.07(48) |
| $C_{440}^0$, GPa | 246.7 | 238.2 | 261.6 |
| $C_{44}^{0\prime}$ | 3.18 | 3.18 | 3.18(5) |
| $C_{660}^0$, GPa | 295.2 | 281.4 | 319.7 |
| $C_{66}^{0\prime}$ | 5.60 | 5.60 | 5.60(13) |

Notes: see the main text for the meaning and references of Landau parameters listed in the first column. Numbers in parentheses represent ±1σ uncertainties.

## 4.2. Al and H effects on the post-stishovite transition boundary

The post-stishovite transition boundary influenced by the Al and/or H substitutions at relevant mantle *P*-*T* conditions can be of direct relevance to our understanding of the depth-dependent distributions of the regional seismic $V_S$ anomalies in the lower mantle as discussed in the introduction. Therefore, we have compared our results with literature data to better evaluate the transition boundary as a function of Al and/or H contents. Based on the Landau modeling at high pressure and 300 K, the $P_C^*$ is at ~21.1 GPa for Al1.3-$SiO_2$ and at ~16.1 GPa for Al2.1-$SiO_2$, which are significantly lower than the $P_C^*$ of 55 GPa in pure-endmember $SiO_2$ stishovite that contains ~19 wt. ppm water (Zhang et al., 2021).

Previous studies have showed that the post-stishovite transition pressure can be lowered by either the Al substitution (Bolfan-Casanova et al., 2009) or water incorporation (Nisr et al., 2017; Umemoto et al., 2016). Al and H incorporations in stishovite can occur via coupled $Al^{3+}$ + $H^+$ for $Si^{4+}$ in the octahedral site, together with $Al^{3+}$ and $O_V^{2+}$ substitution (Pawley et al., 1993). Hydrogen substitution in Al-free stishovite can also occur via $4H^+ \leftrightarrow Si^{4+}$ (Spektor et al., 2011). Importantly, previous studies have found that H solubility increases with the Al substitution in stishovite, but the Al:H ratio in stishovite is mostly near or below 3:1. Therefore, $2Al^{3+} + O_V^{2+} \leftrightarrow 2Si^{4+}$ substitution mechanism is expected to be most prevalent in hydrated Al-bearing stishovite in subducted basalts in the mantle (Pawley et al., 1993). Because our Al-bearing stishovite crystals only contain 0.25-0.27 wt% $H_2O$ with 2.4-3.5 Al/H molar ratios, the $P_C^*$ reduction can thus be mainly attributed to the $2Al^{3+} + O_V^{2+} \leftrightarrow 2Si^{4+}$ effect, together with some contributions from $4H^+ \leftrightarrow Si^{4+}$ substitution. Specifically, the $2Al^{3+} + O_V^{2+} \leftrightarrow 2Si^{4+}$ mechanism softens the stishovite's structure such that the post-stishovite shear distortion occurs more favorably under compression (Lakshtanov et al., 2007a).

Modeling the $P_C^*$ as a function of Al contents using a polynomial function results in Al = $0.0014P_C^{*2} + 0.154P_C^* - 12.705$ where Al is expressed in mol% and the $P_C^*$ is in GPa (Figure 5a). Using a Clapeyron slope of 65 K/GPa from a recent experimental study (Fischer et al., 2018), the post-stishovite transition can be extrapolated to high *P-T* conditions of the lower mantle: the transition pressure could be lowered by approximately 30 GPa in stishovite with 1 mol% Al and by 52 GPa with 3 mol% Al. Along a cold subducting slab which is taken as approximately 500 K colder than a typical normal mantle (Katsura et al., 2010; Tan et al., 2002), the post-stishovite transition is expected to occur at 740 km depth with 3 mol% Al and at 1250 km depth with 1 mol% Al (Figure 5b).

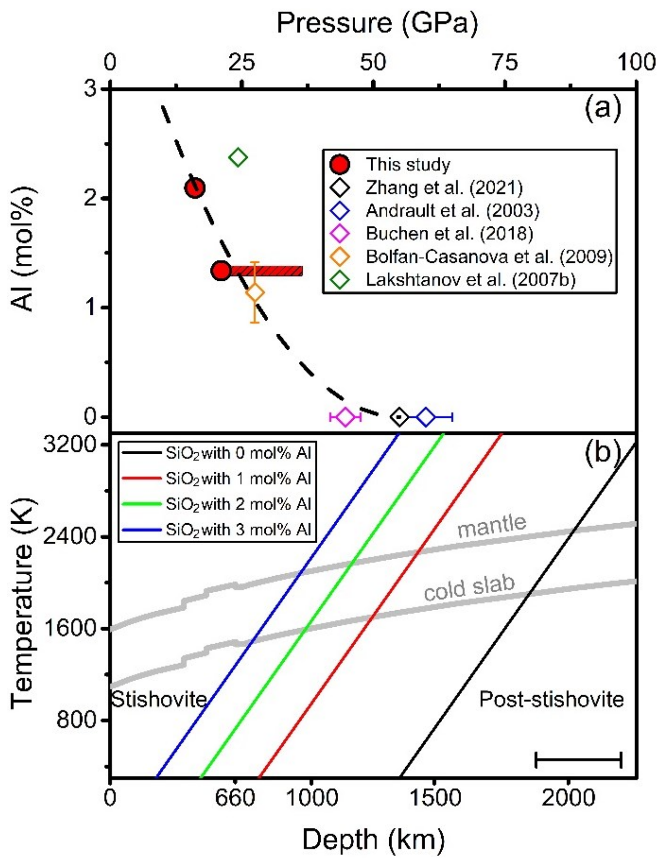


**Figure 5.** Post-stishovite phase transition boundary influenced by Al content in stishovite. (a) The post-stishovite transition pressure as a function of the Al content in mol% at 300 K. The dashed line is the best polynomial fit to our data using 55 GPa for the transition pressure of the pure $SiO_2$ by Zhang et al. (2021). The red shaded area in Al1.3-$SiO_2$ represents a coexistence pressure region where the stishovite and post-stishovite phases coexist (see Figures 2a and 2c). Literature results are also shown for comparison (Andrault et al., 2003; Bolfan-Casanova et al., 2009; Buchen et al., 2018; Lakshtanov et al., 2007b; Zhang et al., 2021). (b) Post-stishovite transition at high *P*-*T* conditions. A Clapeyron slope of 65 K/GPa is used for the post-stishovite transition (Fischer et al.,

2018), where stishovite contains 0 (black), 1 (red), 2 (green), and 3 (blue) mol% Al, respectively. The horizontal bar at the bottom right indicates the coexistence range of the Al-bearing stishovite and post-stishovite phases, which is estimated from the coexistence of the $A_g$ and $A_g^*$ modes in Al1.3-$SiO_2$ (Figures 2a and 2c). A typical normal mantle geotherm (Katsura et al., 2010) and a cold slab geotherm that is 500 K colder than a typical normal mantle geotherm (Tan et al., 2002) are shown as thick gray lines for comparison to the post-stishovite phase boundaries.

### 4.3. Al and H effects on the sound velocities across the post-stishovite transition

Our Landau modeling results provide full elastic moduli of the (Al,H)-bearing stishovite crystals across the post-stishovite transition at high pressure (Figure 6). Examinations of the pressure-dependent $C_{ij}$ in the Al1.3-$SiO_2$ and Al2.1-$SiO_2$ crystals show that they are overall consistent with that of pure $SiO_2$ (Zhang et al., 2021), but the slopes across the transition are quite different. The (Al,H)-bearing stishovite crystals display softer $C_{11}$ and stiffer $C_{12}$ approaching the transition than that in the pure $SiO_2$ stishovite phase. These lead to the convergence of $C_{11}$ and $C_{12}$ at a lower $P_C^*$ in the (Al,H)-bearing system. We should note that the ($C_{11}$-$C_{12}$)/2 constant, which reflects the response of a crystal to deformation caused by shear stress along the [110] direction, is expected to vanish at the transition (Figure 6a). Similarly, the deviations between $C_{12}$ and $C_{22}$ and between $C_{13}$ and $C_{23}$ in the post-stishovite phase becomes larger (Figures 6a and 6b). In addition, our results show an enhanced reduction in the shear modulus and sound velocities (Figures 6c and 6d): the transition correlates with 49% $\mu$ reduction, 29% $V_S$ reduction, and 12% $V_P$ reduction as compared with 45% in $\mu$, 26% in $V_S$, and 10% in $V_P$ reduction in pure $SiO_2$ post-stishovite transition (Zhang et al., 2021).

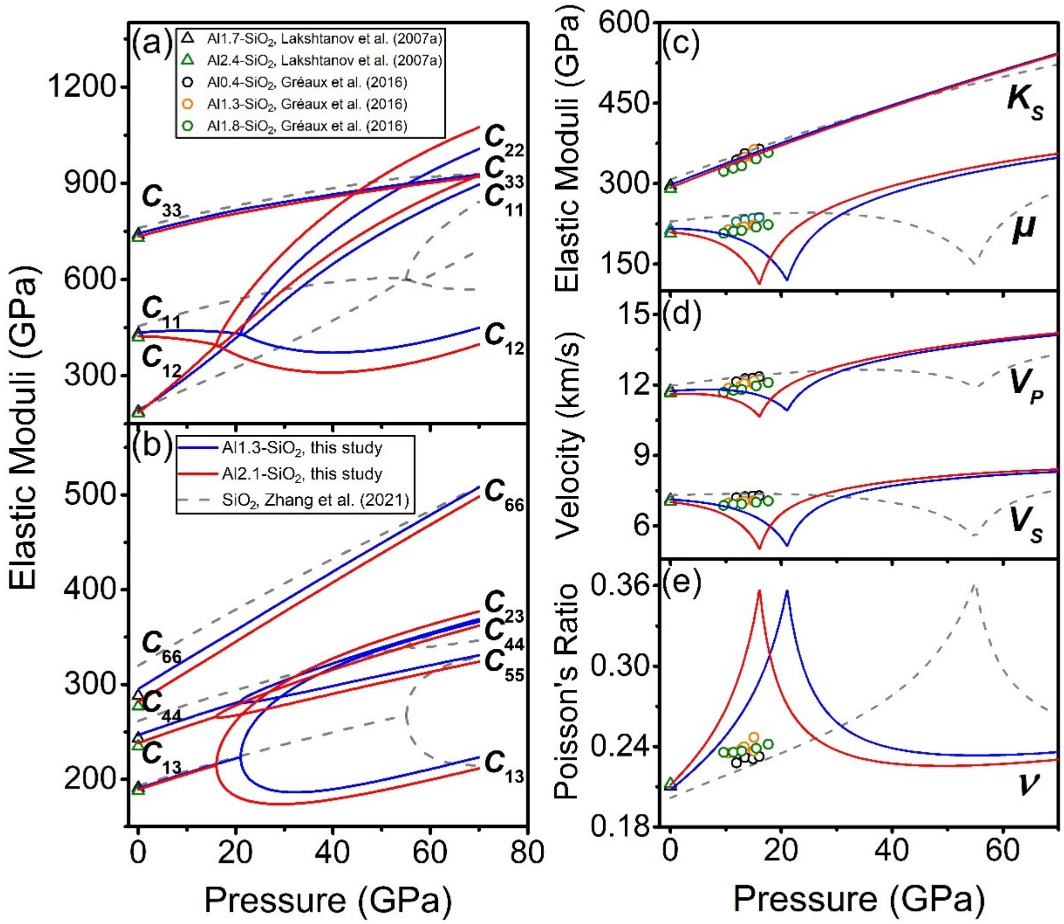


**Figure 6.** Modeled elasticity of the hydrated Al-bearing stishovite and post-stishovite at high pressure. (a) and (b) Elastic moduli $C_{ij}$ of stishovite and post-stishovite at high pressure; (c) adiabatic bulk and shear modulus ($K_S$ and $\mu$) using the Voigt-Reuss-Hill averaging scheme (Hill, 1952); (d) aggregate compressional and shear wave velocities ($V_P$ and $V_S$); (e) Poisson's ratio ($\nu$). The Al1.3-$SiO_2$ (blue lines) and Al2.1-$SiO_2$ (red lines) stishovite crystals undergo the post-stishovite transition at 21.1 and 16.1 GPa, respectively, where their respective $\mu$, $V_P$, and $V_S$ drop drastically. The $\nu$ jumps across the transition. Elasticity data for different compositions are also plotted for comparison (Gréaux et al., 2016; Lakshtanov et al., 2007a; Zhang et al., 2021).

### 4.4. Velocity profiles of subducted MORB across the post-stishovite transition in the lower mantle

The post-stishovite transition is known to occur in the subducted MORB such that sound velocity of the MORB materials can be useful in deciphering seismic results along subducting zone regions in the lower mantle. In our modeling to evaluate the effects of the post-stishovite transition on velocity profiles, we used elasticity of individual mineral phases in an aggregate with MORB composition under relevant *P-T* conditions. The mineralogy in the selected MORB composition contains 20 vol% stishovite, 30 vol% CF, 30 vol% Bgm, and 20 vol% CaPv in the lower mantle (Ishii et al., 2019). Thermoelastic parameters of these mineral phases, except CaPv, in our modeling are taken from Xu et al. (2008), while those for CaPv are taken from Gréaux et al. (2019) and Sun et al. (2016). We should note that the CaPv data by Thomson et al. (2019) are not used here because they measured sound velocities at a nearly constant pressure (~14 GPa) such that some thermoelastic parameters cannot be reliably constrained such as pressure derivatives of $K_S$ and $\mu$. Mie-Grüneisen EOS and finite-strain theory are then used to calculate density $\rho$, bulk modulus $K_S$, and shear modulus $\mu$ of each mineral phase in the MORB mineralogy along a cold subducting slab based on the following equations (Stixrude & Lithgow-Bertelloni, 2005):

$$P = 3K_{T0}f(1+2f)^{5/2}\left[1+\frac{3}{2}(K'_{T0}-4)f\right]+\gamma\rho\Delta\mho_q \tag{5}$$

$$K_S = (1+2f)^{5/2}\left[K_{S0}+(3K_{S0}K'_{S0}-5K_{S0})f+\frac{27}{2}(K_{S0}K'_{S0}-4K_{S0})f^2\right]+(\gamma+1-q)\gamma\rho\Delta\mho_q - \gamma^2\rho\Delta(C_V T) \tag{6}$$

$$\mu = (1+2f)^{5/2}\left[\mu_0+(3K_{S0}\mu'_0-5\mu_0)f+\left(6K_{S0}\mu'_0-24K_{S0}-14\mu_0+\frac{9}{2}K_{S0}K'_{S0}\right)f^2\right]-\eta_S\rho\Delta\mho_q \tag{7}$$

where $f$ is the Eulerian finite strain, $f=\frac{1}{2}\left[(\frac{\rho}{\rho_0})^{2/3}-1\right]$; $\gamma$ is the Grüneisen parameter, $\gamma = \frac{1}{6}(2f+1)(a_1+a_2f)/\left(1+a_1f+\frac{1}{2}a_2f^2\right)$, where $a_1=6\gamma_0$, $a_2=-12\gamma_0+36{\gamma_0}^2-18q\gamma_0$, and $q$ is a constant; $\mho_q$ and $C_V$ are internal energy and isochoric heat capacity, respectively, which can be calculated using the Debye model; $K'_{S0}$ and $\mu'_0$ are the first-order pressure derivative of $K_{S0}$ and $\mu_0$, respectively; $\eta_S$ is the first-order shear strain derivative of $\gamma$, $\eta_S = -\gamma + (2f+1)^2(\gamma_0 + \eta_{S0})/\left(1 + a_1 f + \frac{1}{2}a_2 f^2\right)$; $\Delta$ means the difference between high temperature and 300 K; the subscript '0' denotes the ambient conditions. We should note that the finite-strain model cannot be applied to evaluate the shear softening feature across the post-stishovite ferroelastic transition at high *P*-*T* conditions. Therefore, in addition to the finite-strain modeling, we have evaluated the shear modulus softening, $\Delta\mu$, across the transition at high *P*-*T* using the following equations (Helffrich et al., 2018):

$$\Delta\mu = A_0 \left\{1 - \frac{2}{\pi}\left|arctan\left[\frac{P - P_{tr}(T)}{w}\right]\right|\right\}^2 \quad (8)$$

$$P_{tr}(T) = P_C^* + s(T - 300) \quad (9)$$

where $A_0$ is the maximum shear modulus softening in GPa, $P_{tr}(T)$ is the transition pressure in GPa at *T* in K with a Clapeyron slope $s$ of 1/65 GPa/K, and $w$ is the width of the phase transition in GPa. Fitting our modeled $\mu$ across the post-stishovite transition at 300 K with equations (8) and (9) yields $A_0$ = -148.4(7) GPa and $w$ = 14.7(1) GPa in Al1.3-$SiO_2$ and $A_0$ = -152.4(9) GPa and $w$ = 13.9(2) GPa in Al2.1-$SiO_2$ (Figure 6c). After results have been obtained from these aforementioned modeling efforts, the $\rho$, $K_S$, and $\mu$ for the MORB mineralogy are calculated using the Voigt-Reuss-Hill scheme and volume ratios of the minerals to derive the $V_S$ and $V_P$ profiles of the aggregates in subducted MORB materials in the lower mantle (Figure 7) (Hill, 1952; Ishii et al., 2019).

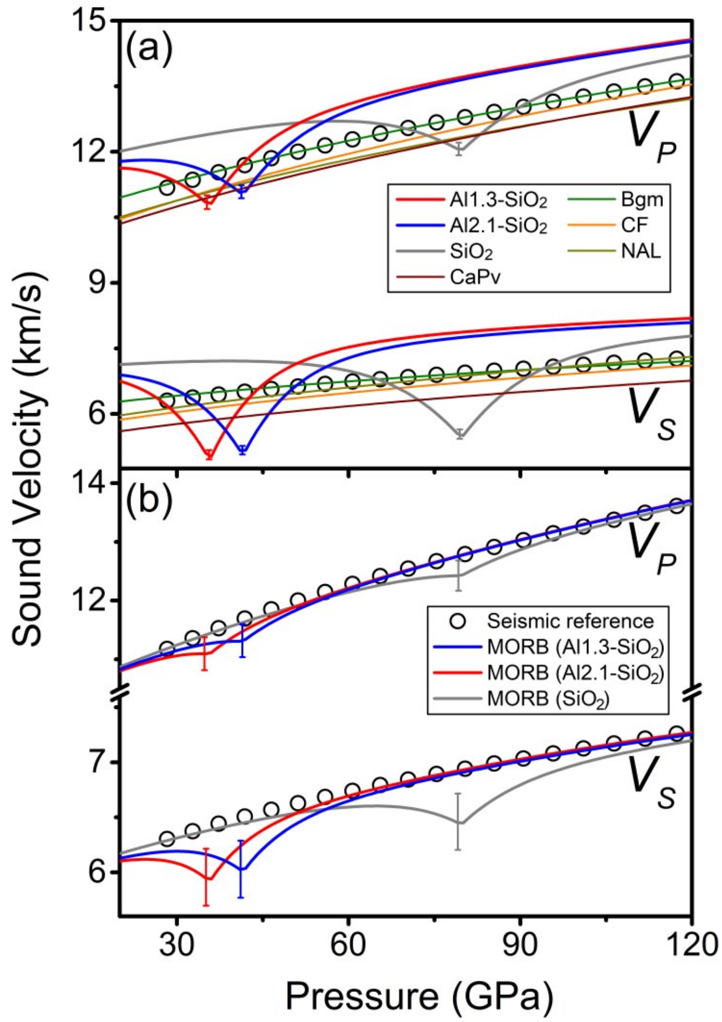


**Figure 7.** Modeled sound velocities of subducted MORB in the lower mantle. The modeled profiles are for a typical cold subducted slab mineralogy which is 500 K colder than a typical normal mantle (Ishii et al., 2019; Katsura et al., 2010; Tan et al., 2002). (a) $V_P$ and $V_S$ profile of MORB materials. The $SiO_2$ with different Al contents and other MORB materials are shown as lines with different colors (Wu et al., 2016; Xu et al., 2008). (b) Velocity models in the MORB mineralogy with 20 vol% stishovite with Al1.3-$SiO_2$ (blue lines), Al2.1-$SiO_2$ (red lines), or pure $SiO_2$ composition (gray lines). Propagated standard errors (±1σ uncertainties) in the model are shown as vertical bars with the same color as the corresponding lines in (a) and (b). Reference seismic profiles plotted as open circles represent seismic velocities in cold subduction regions that are about 1% higher than PREM at the same depth (Dziewonski & Anderson, 1981).

## 5. Geophysical implication

Short-period seismic wave studies indicate that small-scale seismic heterogeneities are distributed ubiquitously throughout the whole mantle (Hedlin et al., 1997). Many of these small-scale seismic heterogeneities have *S*-to-*P* or *P*-to-*P* wave scattering associated with a strong negative $V_S$ anomaly from top to mid lower mantle beneath South America (Haugland et al., 2017), Tonga (Kaneshima, 2013, 2018, 2019; Vinnik et al., 2001), Mariana (Kaneshima & Helffrich, 1999; Niu et al., 2003), and Japan sea (Li & Yuen, 2014; Niu, 2014) (Figure 8a). Some studies further suggest that some regions at ~1000 km depth are about 2-9% denser than the surrounding lower mantle (Niu, 2014; Niu et al., 2003). These observations may be indicative of ancient subducted MORB with ~20 vol% Al-bearing stishovite that is up to ~5.5% denser than a representative pyrolite mineralogy model above 25 GPa (~700 km depth) (Hirose et al., 2005; Ishii et al., 2019). The subducted MORB containing abundant stishovite is also rigid enough to survive mantle convection over long geological history (Kaneshima, 2016; Xu et al., 2017). A trace-element geochemistry model has indicated that bulk silicate Earth consists of 15 wt% MORB materials which are largely dispersed as small-scale seismic scatterers in the lower mantle (Helffrich et al., 2018).

The post-stishovite transition has been considered to be a possible cause for the existence of the aforementioned regional seismic shear wave anomalies (Kaneshima, 2018; Lakshtanov et al., 2007b). Here we use our results to provide new constrains on sound velocity profiles across the Al,H-bearing post-stishovite transition at high *P*-*T*. Based on seismic velocities in cold subduction regions (such as Tonga) from a representative three-dimensional global tomography model (Lu et al., 2019), typical $V_S$ and $V_P$ profiles along subduction slabs are ~1% higher than that in the preliminary reference Earth model (PREM) at the same depth (Dziewonski & Anderson, 1981). Our modeled results show that $V_P$ and $V_S$ profiles of Al-bearing stishovite and post-stishovite phases away from the transition are much higher than those of other minerals in the MORB materials, including Bgm, CaPv, CF, and NAL, that are similar to or lower than the typical $V_P$ and $V_S$ profiles in cold subduction regions (Figure 7a). The high $V_S$ and $V_P$ profiles of 20 vol% stishovite/post-stishovite in subducted MORB mineralogy would particularly compensate for the lowest $V_S$ and $V_P$ profiles of 20 vol% CaPv among MORB components. That is, the $V_S$ and $V_P$ profiles of the modeled MORB mineralogy with 20 vol% stishovite/post-stishovite and 20 vol% CaPv would display velocity profiles that are consistent with the typical cold-slab velocity profiles (Figure 7b). Across the post-stishovite transition, however, both $V_S$ and $V_P$ of stishovite drastically soften, but the magnitude of the $V_S$ softening is much stronger than the $V_P$ softening (Figure 7a). That is, the $V_S$ of stishovite across the transition is ~15% maximum lower than that of CaPv, but the $V_P$ is similar to that of CaPv at the same depths (Figure 7a). This leads to a distinguishable negative $V_S$ anomaly of the subducted MORB materials but no visible $V_P$ anomalies within uncertainties of our model as compared with the surrounding mantle (Figure 7b). Specifically, The maximum negative $V_S$ contrast (d$V_{S,max}$) at the post-stishovite transition boundary is -7.5(±4.2)% for Al1.3-$SiO_2$ and -7.7(±4.3)% for Al2.1-$SiO_2$ crystal (Figure 8a).

We have also taken the effects of Al content on the phase boundary and sound velocity profiles of the post-stishovite transition in the lower mantle into consideration using our experimental and modeled results. Previous studies have showed that the Al content in MORB materials can vary from ~4.3 to 8.1 mol% (Gale et al., 2013), which in turn affects the amount of Al in natural stishovite. Considering MORB materials with a typical ~6.8 mol% Al, stishovite is expected to contain ~1.3 mol% Al in the subducted MORB materials from 800 to 1600 km depth (Figure S2). For a typical MORB with 20 vol% stishovite, the post-stishovite transition would occur at ~1064 km depth with ~-7% d$V_{S,max}$. The transition depth can shift from 660 km depth at the topmost lower mantle for stishovite with 3.5 mol% Al to approximately 1860 km at mid lower-mantle depth for pure $SiO_2$ stishovite (Figure 8b). The d$V_{S,max}$ for these Al-bearing post-stishovite transitions range from approximately -8(4)% at 660 km depth to -7(4)% at 1860 km depth. That is, the d$V_{S,max}$ remains almost constant within uncertainties (Figure 8a). We should note that the post-stishovite transition is a ferroelastic that occurs continuously through lattice distortions under pressure. Therefore, the $V_S$ softening exists over an extended pressure range (or depth) across the transition (Figure 7). This effect, together with Al,H-influenced post-stishovite transition pressure, can broaden the geophysical consequences of the transition and help explain depth-dependent seismic wave $V_S$ anomalies in a number of representative subduction regions including the Tonga subduction zone (Figure 8a).

Seismic studies have reported forty-one *S*-to-*P* wave scatterers in the vicinity of Tonga slab which has been subducting since 100 Myr ago and currently reaching the mid lower mantle depths (Kaneshima, 2013, 2018, 2019). Analysis of these *S*-to-*P* scatterings has provided geometries, velocity anomalies, and locations of these small-scale heterogeneities. These scatterers are interpreted as thin slab planes with a steep dip angle which are tens of kilometers away from the Tonga slab. These observations also match the size, shape, viscosity, and location of the subducted MORB (Fukao & Obayashi, 2013; Xu et al., 2017). They exhibit strong $V_S$ anomalies of -7(4)% as compared to the surrounding mantle at 700-1900 km depth. The magnitude of the seismically observed $V_S$ anomalies in these regions is in general consistent with our modeled $V_S$ anomaly in MORB with 20% silica undergoing the post-stishovite transition (Figure 8a). The $V_S$ anomalies have been detected at a wide depth range from the topmost to mid lower mantle, which can be interpreted as a result of the Al-dependent post-stishovite transition due to heterogeneous Al distributions in subducted MORB materials as well as the ferroelastic feature of $V_S$ reduction over a broad pressure range (Figure 8b). Seismic observations also show that the number of these anomalies decreases with depth and the majority of these seismic scatterers (~85%) occurs above 1600 km depth (Kaneshima, 2013, 2018, 2019). These observations are in general consistent with the broad $V_S$ softening feature across the Al,H-bearing post-stishovite transition boundary.

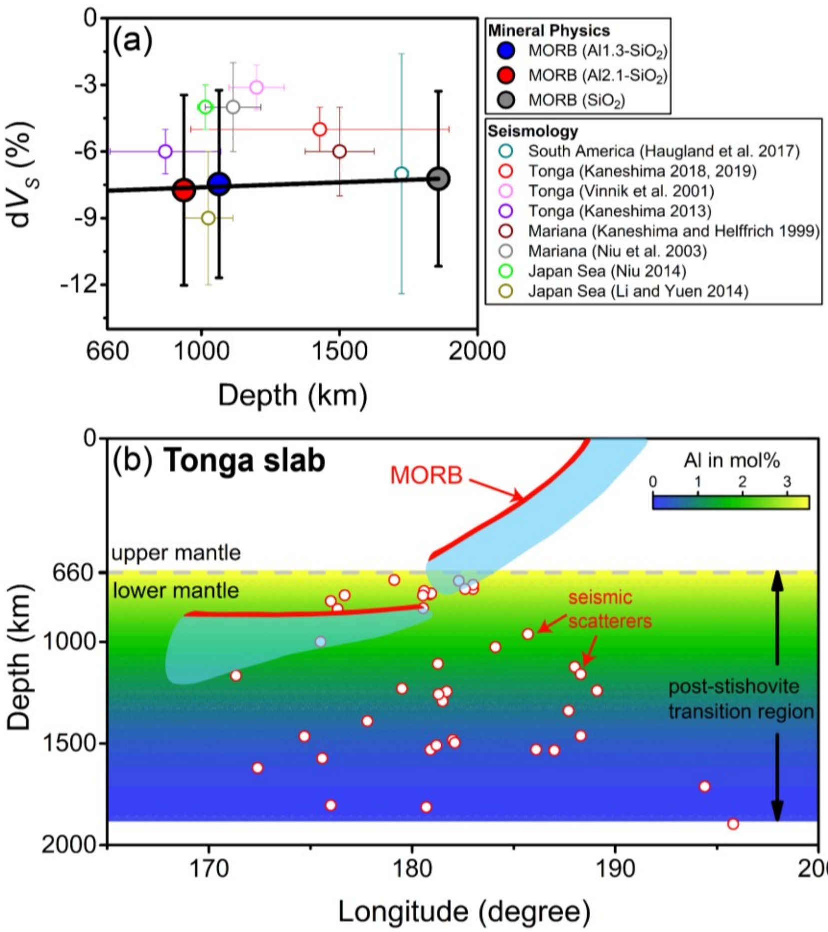


**Figure 8.** Seismic observations and mineral physics modeling of the depth-dependent $V_S$ anomalies (d$V_S$) in the lower mantle. (a) d$V_S$ observations of regional seismic $V_S$ anomalies around subducting slabs at various depths are plotted as open circles. 20 vol% stishovite in a subducted MORB composition is used in our mineral physics model to account for the maximum $V_S$ anomaly (d$V_{S,max}$) across the post-stishovite transition shown as solid circles. The d$V_{S,max}$ in % is calculated using the formula of $(V_{S,MORB}-V_{S,cold\ slab})/(V_{S,MORB}+V_{S,cold\ slab})\times200$, where the $V_{S,cold\ slab}$ value is higher than the $V_S$ of PREM by 1% at the same depth (Dziewonski & Anderson, 1981) (Figure 7b). The solid line is the best linear fit to our modeled data. Literature data for seismic observations

include Haugland et al. (2017), Kaneshima (2018, 2019), Vinnik et al. (2001), Kaneshima (2013), Kaneshima and Helffrich (1999), Niu et al. (2003), Niu (2014), and Li and Yuen (2014). Note that some of these studies have only reported lower bound of the $V_S$ anomaly (Kaneshima, 2013, 2018; Kaneshima & Helffrich, 1999). (b) Depth-longitude schematics for the seismic d$V_S$ anomalies and the post-stishovite transition along the Tonga subduction region. The color shaded area represents the post-stishovite transition region scaled with the Al content in a color scale shown on the top right. Reported seismic $V_S$ anomalies (red open circles) with different latitudes in the Tonga region are projected onto the two-dimensional schematic (Kaneshima, 2009, 2013, 2018, 2019; Kaneshima & Helffrich, 2010). The geometry and position of the Tonga subducting slab are drawn according to previous seismic images (Fukao & Obayashi, 2013).

Our results can also have implications to our understanding of the water circulation and storage in the deep mantle. MORB materials can undergo hydrothermal processes in the deep ocean-crust interface and be enriched with water and other volatiles in the alternation processes. The subduction of MORB materials, together with hydrated sediments, can bring a certain amount of water into the mantle. As subduction occurs deeper, the top sedimental and basaltic layers of slabs become too hot and will likely release most of the water (van Keken et al., 2011), but some water can remain in the NAMs. Stishovite is one of the NAMs and can accommodate a certain amount of water in its lattice along the subduction processes (Lin et al., 2019; Litasov et al., 2007; Ohtani, 2020). As the subducting slabs reach the 660-km boundary layer in some subduction regions, dehydration-induced partial melting can occur at the top of the lower mantle. This can lead to ponding of partial melts in the region that is observed as low $V_S$ regions in seismic studies (Liu et al., 2016; Schmandt et al., 2014). A recent study even suggests that the partial melting process can produce Al-bearing stishovite with approximately 700 wt. ppm $H_2O$ in the upper part of lower mantle (Amulele et al., 2021). Our Al-bearing stishovite can contain 0.25 and 0.27 wt% $H_2O$ with an Al:H ratio close to 3:1 (Figure 1d). Using 3:1 for the Al:H ratio in natural stishovite in a typical

MORB composition, stishovite with 1.3 mol% Al would contain approximately 0.65 mol% H (or 0.3 wt% $H_2O$) in the upper part of the lower mantle. The 0.3 wt% $H_2O$ in stishovite is significantly larger than the water solubility of ~0.1 wt% in other MORB components such as Bgm and NAL phase (Fu et al., 2019; Wu et al., 2016), making the Al-bearing stishovite a plausible water carrier along the subduction slabs into the lower mantle.

Water enrichments in silica-rich materials may further explain the distribution of regional seismic $V_S$ anomalies over a wide depth range. Previous diffusion experiments show that dry stishovite is much more viscous than bridgmanite in the upper part of the lower mantle (Xu et al., 2017). However, the water incorporation has been shown to increase diffusion creep in NAMs in previous studies (Karato & Wu, 1993), but the effect of hydration on the rheology of stishovite remains uncertain. Assuming that water substitution in stishovite can reduce the rheology of stishovite and possibly post-stishovite, hydrated silica-rich material could become relatively detachable from subducted slab and be locally segregated from the topmost to mid lower mantle regions (Kaneshima, 2019). Previous studies have showed that hydration in stishovite can signficantly enhance its electrical conductivity by two orders of magnitude at 12 GPa and 1900 K (Yoshino et al., 2014). This may help explain electromagnetic observations of high electrical conductivity regions along circum-Pacific subducting slabs in the uppermost lower mantle (Kelbert et al., 2009), where many subduction slabs are found to be stagnant (Fukao & Obayashi, 2013).

## 6. Conclusion

We have studied the vibrational Raman modes and lattice parameters of two Al-bearing stishovite crystals, Al1.3-$SiO_2$ with 0.55 mol% H and Al2.1-$SiO_2$ with 0.59 mol% H, across the post-stishovite transition at high pressure. The experimental results are used to evaluate the Al and Al/H substitutional effects on the post-stishovite phase boundary and the elasticity across the post-stishovite transition. Landau theory modeling of the experimental data is used to derive the transition pressure and full elasticity across the transition, where the soft $B_{1g}$ mode becomes the hard $A_g$ mode, the *a* axis splits into the *a* and *b* axis, the $(C_{11}-C_{12})/2$ approaches zero, and the $V_S$ displays -29% softening. The Al and H incorporation reduces the transition pressure to 21.1 GPa in Al1.3-$SiO_2$ and 16.1 GPa in Al2.1-$SiO_2$. We have modeled high *P*-*T* phase boundary and elasticity of stishovite and post-stishovite for a MORB mineralogy with 20 vol% stishovite. For a typical MORB composition where stishovite is expected to contain 1.3 mol% Al, the post-stishovite transition can cause for -7(4)% d$V_{S,max}$ in subducted MORB at 1064 km depth. These results help explain depth-dependent $V_S$ anomaly distributions of some regional small-scale scatterers especially for the *S*-to-*P* scattering along the Tonga subduction region. The Al-bearing stishovite can also accommodate approximately 0.3 wt% $H_2O$ via the coupled substitution mechanism of $Al^{3+} + H^+ \leftrightarrow Si^{4+}$ in the upper part of the lower mantle. The lattice-bonded water is expected to remain stable in the post-stishovite phase. The water in stishovite and post-stishovite phases could affect rheology and electrical conductivity of silica-rich materials in the region.

**Conflict of Interest**

The authors declare that they have no known competing interests or personal relationships that could have influenced the work in this paper.

**Data Availability Statement**

EPMA results are listed in Table S1. Raman data for Figure 2 are available in Table S2 to S4. XRD data for Figure 3 are available in Table S5 to S7. All these data can also be downloaded online (http:XXX).

## Acknowledgements

We thank N. Purevjav for her assistances on the synthesis and characterization of the single-crystal stishovite. We also thank Jennifer Kung, Vincent Jian and Ching-Chien Li for their assistance in FTIR measurements. Diffraction experiments were performed at 13ID-D, GSECARS. GSECARS was supported by the National Science Foundation (EAR-0622171) and U.S. Department of Energy (DE-FG0294ER14466) under contract DE-AC0206CH11357. J.F. Lin acknowledges support from Geophysics Program of the U.S. National Science Foundation (EAR-1916941 and EAR-2001381) and the Joint-Use User Program of the Institute for Planetary Materials, Okayama University. T. Okuchi acknowledges support from JSPS KAKENHI (17H01172).

## References

Amulele, G., Karato, S.-i., & Girard, J. (2021). Melting of bridgmanite under hydrous shallow lower mantle conditions.

Andrault, D., Angel, R. J., Mosenfelder, J. L., & Bihan, T. L. (2003). Equation of state of stishovite to lower mantle pressures. *American Mineralogist, 88*(2-3), 301-307.

Asahara, Y., Hirose, K., Ohishi, Y., Hirao, N., Ozawa, H., & Murakami, M. (2013). Acoustic velocity measurements for stishovite across the post-stishovite phase transition under deviatoric stress: Implications for the seismic features of subducting slabs in the mid-mantle. *American Mineralogist, 98*(11-12), 2053-2062.

Birch, F. (1947). Finite elastic strain of cubic crystals. *Physical review, 71*(11), 809.

Bolfan-Casanova, N., Andrault, D., Amiguet, E., & Guignot, N. (2009). Equation of state and post-stishovite transformation of Al-bearing silica up to 100GPa and 3000K. *Physics of the Earth and Planetary Interiors, 174*(1), 70-77.

Buchen, J., Marquardt, H., Schulze, K., Speziale, S., Boffa Ballaran, T., Nishiyama, N., & Hanfland, M. (2018). Equation of State of Polycrystalline Stishovite Across the Tetragonal-Orthorhombic Phase Transition. *Journal of Geophysical Research: Solid Earth, 123*(9), 7347-7360.

Carpenter, M. A., Hemley, R. J., & Mao, H. k. (2000). High-pressure elasticity of stishovite and the P42/mnm⇌ Pnnm phase transition. *Journal of Geophysical Research: Solid Earth, 105*(B5), 10807-10816.

Dziewonski, A. M., & Anderson, D. L. (1981). Preliminary reference Earth model. *Physics of the Earth and Planetary Interiors, 25*(4), 297-356.

Fei, Y., Ricolleau, A., Frank, M., Mibe, K., Shen, G., & Prakapenka, V. (2007). Toward an internally consistent pressure scale. *Proceedings of the National Academy of Sciences, 104*(22), 9182-9186.

Fischer, R. A., Campbell, A. J., Chidester, B. A., Reaman, D. M., Thompson, E. C., Pigott, J. S., et al. (2018). Equations of state and phase boundary for stishovite and CaCl2-type SiO2. *American Mineralogist, 103*(5), 792-802.

Fu, S., Yang, J., Karato, S. i., Vasiliev, A., Presniakov, M. Y., Gavrilliuk, A. G., et al. (2019). Water concentration in single-crystal (Al, Fe)-bearing bridgmanite grown from the hydrous melt: implications for dehydration melting at the topmost lower mantle. *Geophysical Research Letters*.

Fukao, Y., & Obayashi, M. (2013). Subducted slabs stagnant above, penetrating through, and trapped below the 660 km discontinuity. *Journal of Geophysical Research: Solid Earth, 118*(11), 5920-5938.

Gale, A., Dalton, C. A., Langmuir, C. H., Su, Y., & Schilling, J. G. (2013). The mean composition of ocean ridge basalts. *Geochemistry, Geophysics, Geosystems, 14*(3), 489-518.

Gréaux, S., Irifune, T., Higo, Y., Tange, Y., Arimoto, T., Liu, Z., & Yamada, A. (2019). Sound velocity of CaSiO 3 perovskite suggests the presence of basaltic crust in the Earth's lower mantle. *Nature, 565*(7738), 218.

Gréaux, S., Kono, Y., Wang, Y., Yamada, A., Zhou, C., Jing, Z., et al. (2016). Sound velocities of aluminum-bearing stishovite in the mantle transition zone. *Geophysical Research Letters, 43*(9), 4239-4246.

Haugland, S. M., Ritsema, J., Kaneshima, S., & Thorne, M. S. (2017). Estimate of the Rigidity of Eclogite in the Lower Mantle From Waveform Modeling of Broadband S-to-P Wave Conversions. *Geophysical Research Letters, 44*(23), 11,778-711,784.

Hedlin, M. A., Shearer, P. M., & Earle, P. S. (1997). Seismic evidence for small-scale heterogeneity throughout the Earth's mantle. *Nature, 387*(6629), 145.

Helffrich, G., Ballmer, M. D., & Hirose, K. (2018). Core-Exsolved SiO2 Dispersal in the Earth's Mantle. *Journal of Geophysical Research: Solid Earth, 123*(1), 176-188.

Hemley, R., Shu, J., Carpenter, M., Hu, J., Mao, H., & Kingma, K. (2000). Strain/order parameter coupling in the ferroelastic transition in dense SiO2. *Solid State Communications, 114*(10), 527-532.

Hill, R. (1952). The elastic behaviour of a crystalline aggregate. *Proceedings of the Physical Society. Section A, 65*(5), 349.

Hirose, K., Takafuji, N., Sata, N., & Ohishi, Y. (2005). Phase transition and density of subducted MORB crust in the lower mantle. *Earth and Planetary Science Letters, 237*(1-2), 239-251.

Irifune, T., Shinmei, T., McCammon, C. A., Miyajima, N., Rubie, D. C., & Frost, D. J. (2010). Iron partitioning and density changes of pyrolite in Earth's lower mantle. *Science, 327*(5962), 193-195.

Ishii, T., Kojitani, H., & Akaogi, M. (2019). Phase Relations of Harzburgite and MORB up to the Uppermost Lower Mantle Conditions: Precise Comparison With Pyrolite by Multisample Cell High-Pressure Experiments With Implication to Dynamics of Subducted Slabs. *Journal of Geophysical Research: Solid Earth*.

Kaneshima, S. (2009). Seismic scatterers at the shallowest lower mantle beneath subducted slabs. *Earth and Planetary Science Letters, 286*(1-2), 304-315.

Kaneshima, S. (2013). Lower mantle seismic scatterers below the subducting Tonga slab: Evidence for slab entrainment of transition zone materials. *Physics of the Earth and Planetary Interiors, 222*, 35-46.

Kaneshima, S. (2016). Seismic scatterers in the mid-lower mantle. *Physics of the Earth and Planetary Interiors, 257*, 105-114.

Kaneshima, S. (2018). Seismic scatterers in the mid-lower mantle beneath Tonga-Fiji. *Physics of the Earth and Planetary Interiors, 274*, 1-13.

Kaneshima, S. (2019). Seismic scatterers in the lower mantle near subduction zones. *Geophysical Journal International, 218*(3), 1873-1891.

Kaneshima, S., & Helffrich, G. (1999). Dipping low-velocity layer in the mid-lower mantle: evidence for geochemical heterogeneity. *Science, 283*(5409), 1888-1892.

Kaneshima, S., & Helffrich, G. (2010). Small scale heterogeneity in the mid-lower mantle beneath the circum-Pacific area. *Physics of the Earth and Planetary Interiors, 183*(1-2), 91-103.

Karato, S.-i., & Wu, P. (1993). Rheology of the upper mantle: A synthesis. *Science, 260*(5109), 771-778.

Karki, B. B., Stixrude, L., & Crain, J. (1997). Ab initio elasticity of three high-pressure polymorphs of silica. *Geophysical Research Letters, 24*(24), 3269-3272.

Katsura, T., Yoneda, A., Yamazaki, D., Yoshino, T., & Ito, E. (2010). Adiabatic temperature profile in the mantle. *Physics of the Earth and Planetary Interiors, 183*(1-2), 212-218.

Kelbert, A., Schultz, A., & Egbert, G. (2009). Global electromagnetic induction constraints on transition-zone water content variations. *Nature, 460*(7258), 1003.

Kingma, K. J., Cohen, R. E., Hemley, R. J., & Mao, H.-k. (1995). Transformation of stishovite to a denser phase at lower-mantle pressures. *Nature, 374*(6519), 243.

Lakshtanov, D. L., Litasov, K. D., Sinogeikin, S. V., Hellwig, H., Li, J., Ohtani, E., & Bass, J. D. (2007a). Effect of Al3+ and H+ on the elastic properties of stishovite. *American Mineralogist, 92*(7), 1026-1030.

Lakshtanov, D. L., Sinogeikin, S. V., Litasov, K. D., Prakapenka, V. B., Hellwig, H., Wang, J., et al. (2007b). The post-stishovite phase transition in hydrous alumina-bearing SiO2 in the lower mantle of the earth. *Proceedings of the National Academy of Sciences, 104*(34), 13588-13590.

Li, B., Rigden, S. M., & Liebermann, R. C. (1996). Elasticity of stishovite at high pressure. *Physics of the Earth and Planetary Interiors, 96*(2-3), 113-127.

Li, J., & Yuen, D. A. (2014). Mid-mantle heterogeneities associated with Izanagi plate: Implications for regional mantle viscosity. *Earth and Planetary Science Letters, 385*, 137-144.

Lin, Y., Hu, Q., Meng, Y., Walter, M., & Mao, H.-K. (2019). Evidence for the stability of ultrahydrous stishovite in Earth's lower mantle. *Proceedings of the National Academy of Sciences*.

Litasov, K. D., Kagi, H., Shatskiy, A., Ohtani, E., Lakshtanov, D. L., Bass, J. D., & Ito, E. (2007). High hydrogen solubility in Al-rich stishovite and water transport in the lower mantle. *Earth and Planetary Science Letters, 262*(3), 620-634.

Liu, Z., Park, J., & Karato, S. i. (2016). Seismological detection of low-velocity anomalies surrounding the mantle transition zone in Japan subduction zone. *Geophysical Research Letters, 43*(6), 2480-2487.

Lu, C., Grand, S. P., Lai, H., & Garnero, E. J. (2019). TX2019slab: A New P and S Tomography Model Incorporating Subducting Slabs. *Journal of Geophysical Research: Solid Earth*.

Nisr, C., Leinenweber, K., Prakapenka, V., Prescher, C., Tkachev, S., & Dan Shim, S. H. (2017). Phase transition and equation of state of dense hydrous silica up to 63 GPa. *Journal of Geophysical Research: Solid Earth*.

Niu, F. (2014). Distinct compositional thin layers at mid-mantle depths beneath northeast China revealed by the USArray. *Earth and Planetary Science Letters, 402*, 305-312.

Niu, F., Kawakatsu, H., & Fukao, Y. (2003). Seismic evidence for a chemical heterogeneity in the midmantle: A strong and slightly dipping seismic reflector beneath the Mariana subduction zone. *Journal of Geophysical Research: Solid Earth, 108*(B9).

Ohtani, E. (2020). The role of water in Earth's mantle. *National Science Review, 7*(1), 224-232.

Okuchi, T., Purevjav, N., Tomioka, N., Lin, J.-F., Kuribayashi, T., Schoneveld, L., et al. (2015). Synthesis of large and homogeneous single crystals of water-bearing minerals by slow cooling at deep-mantle pressures. *American Mineralogist, 100*(7), 1483-1492.

Ono, S., Ito, E., & Katsura, T. (2001). Mineralogy of subducted basaltic crust (MORB) from 25 to 37 GPa, and chemical heterogeneity of the lower mantle. *Earth and Planetary Science Letters, 190*(1), 57-63.

Paterson, M. (1982). The determination of hydroxyl by infrared absorption in quartz, silicate glasses and similar materials. *Bull Mineral, 105*, 20-29.

Pawley, A. R., McMillan, P. F., & Holloway, J. R. (1993). Hydrogen in stishovite, with implications for mantle water content. *SCIENCE-NEW YORK THEN WASHINGTON-, 261*, 1024-1024.

Prescher, C., & Prakapenka, V. B. (2015). DIOPTAS: a program for reduction of two-dimensional X-ray diffraction data and data exploration. *High Pressure Research, 35*(3), 223-230.

Ringwood, A. E. (1975). Composition and Petrology of the Earth's Mantle. *MacGraw-Hill, 618*.

Rost, S., Garnero, E. J., & Williams, Q. (2008). Seismic array detection of subducted oceanic crust in the lower mantle. *Journal of Geophysical Research: Solid Earth, 113*(B6).

Salje, E. (1990). Phase transitions in ferroelastic and co-elastic crystals. *Ferroelectrics, 104*(1), 111-120.

Schmandt, B., Jacobsen, S. D., Becker, T. W., Liu, Z., & Dueker, K. G. (2014). Dehydration melting at the top of the lower mantle. *Science, 344*(6189), 1265-1268.

Shieh, S. R., Duffy, T. S., & Li, B. (2002). Strength and Elasticity of S i O 2 across the Stishovite–C a C l 2-type Structural Phase Boundary. *Physical review letters, 89*(25), 255507.

Spektor, K., Nylen, J., Stoyanov, E., Navrotsky, A., Hervig, R. L., Leinenweber, K., et al. (2011). Ultrahydrous stishovite from high-pressure hydrothermal treatment of SiO2. *Proceedings of the National Academy of Sciences, 108*(52), 20918-20922.

Stixrude, L., & Lithgow-Bertelloni, C. (2005). Thermodynamics of mantle minerals—I. Physical properties. *Geophysical Journal International, 162*(2), 610-632.

Sun, N., Mao, Z., Yan, S., Wu, X., Prakapenka, V. B., & Lin, J. F. (2016). Confirming a pyrolitic lower mantle using self-consistent pressure scales and new constraints on CaSiO3 perovskite. *Journal of Geophysical Research: Solid Earth, 121*(7), 4876-4894.
Tan, E., Gurnis, M., & Han, L. (2002). Slabs in the lower mantle and their modulation of plume formation. *Geochemistry, Geophysics, Geosystems, 3*(11), 1-24.
Thomson, A., Crichton, W., Brodholt, J., Wood, I., Siersch, N., Muir, J., et al. (2019). Seismic velocities of CaSiO 3 perovskite can explain LLSVPs in Earth's lower mantle. *Nature, 572*(7771), 643-647.
Umemoto, K., Kawamura, K., Hirose, K., & Wentzcovitch, R. M. (2016). Post-stishovite transition in hydrous aluminous SiO 2. *Physics of the Earth and Planetary Interiors, 255*, 18-26.
van Keken, P. E., Hacker, B. R., Syracuse, E. M., & Abers, G. A. (2011). Subduction factory: 4. Depth-dependent flux of H2O from subducting slabs worldwide. *Journal of Geophysical Research: Solid Earth, 116*(B1).
Vinnik, L., Kato, M., & Kawakatsu, H. (2001). Search for seismic discontinuities in the lower mantle. *Geophysical Journal International, 147*(1), 41-56.
Wang, W., Xu, Y., Sun, D., Ni, S., Wentzcovitch, R., & Wu, Z. (2020). Velocity and density characteristics of subducted oceanic crust and the origin of lower-mantle heterogeneities. *Nature Communications, 11*(1), 1-8.
Wu, Y., Yang, J., Wu, X., Song, M., Yoshino, T., Zhai, S., et al. (2016). Elasticity of single-crystal NAL phase at high pressure: A potential source of the seismic anisotropy in the lower mantle. *Journal of Geophysical Research: Solid Earth, 121*(8), 5696-5707.
Xu, F., Yamazaki, D., Sakamoto, N., Sun, W., Fei, H., & Yurimoto, H. (2017). Silicon and oxygen self-diffusion in stishovite: Implications for stability of SiO2-rich seismic reflectors in the mid-mantle. *Earth and Planetary Science Letters, 459*, 332-339.
Xu, W., Lithgow-Bertelloni, C., Stixrude, L., & Ritsema, J. (2008). The effect of bulk composition and temperature on mantle seismic structure. *Earth and Planetary Science Letters, 275*(1-2), 70-79.
Yang, J., Tong, X., Lin, J.-F., Okuchi, T., & Tomioka, N. (2015). Elasticity of ferropericlase across the spin crossover in the Earth's lower mantle. *Scientific reports, 5*.
Yang, R., & Wu, Z. (2014). Elastic properties of stishovite and the CaCl 2-type silica at the mantle temperature and pressure: An ab initio investigation. *Earth and Planetary Science Letters, 404*, 14-21.
Yoshino, T., Shimojuku, A., & Li, D. (2014). Electrical conductivity of stishovite as a function of water content. *Physics of the Earth and Planetary Interiors, 227*, 48-54.
Zedgenizov, D., Shatsky, V., Panin, A., Evtushenko, O., Ragozin, A., & Kagi, H. (2015). Evidence for phase transitions in mineral inclusions in superdeep diamonds of the São Luiz deposit (Brazil). *Russian Geology and Geophysics, 56*(1-2), 296-305.
Zhang, Y., Fu, S., Wang, B., & Lin, J.-F. (2021). Elasticity of a Pseudoproper Ferroelastic Transition from Stishovite to Post-Stishovite at High Pressure. *Physical review letters, 126*(2), 025701.